Title: Nucleation and growth of iron- and phosphorus-rich phases from a modified steelmaking waste slag

Authors: Juncheng Li [a, *], Guoxuan Li [a], Feng Qiu [a], Rong Wang [a], Jinshan Liang [a], Yi Zhong [a], Dong Guan [a], Seetharaman Sridhar [b] and Zushu Li [c]

[a] School of Material Science and Engineering, Jiangsu University, Zhenjiang, 212013, P. R. China

[b] Engineering of Matter, Transport and Energy, Arizona State University, Tempe, AZ 85287, USA

[c] WMG, the University of Warwick, Coventry, CV4 7AL UK

Files: Cover Letter; Manuscript; Declaration of Interest Statement

[*] Corresponding author.
E-mail address: leejc2011@163.com (J Li).

Abstract

Recovering the iron (Fe) and phosphorus (P) contained in steelmaking slags not only conserves natural resources, but also supports achieving the sustainability of the steel industry. We had previously found the possibility of recovering Fe and P resources contained in steelmaking slags by adjusting oxygen partial pressure and adding modifier B_2O_3. As a fundamental study for efficiently recovering Fe and P from steelmaking slag, in this study, the crystallization behaviors of the CaO-SiO_2-FeO-P_2O_5-B_2O_3 melt has been observed in situ, through a confocal scanning laser microscope. The kinetics of nucleation and growth of Fe- and P-rich phases have been calculated using a classical crystallization kinetic theory. During cooling, a Fe_3O_4 phase with faceted morphology was observed as the 1st precipitated phase in the isothermal interval of 1300 ℃-1150 ℃, while $Ca_{10}P_6O_{25}$, with rod-shaped morphology, was found to be the 2nd phase to precipitate in the interval 1150 ℃ -1000 ℃. The crystallization abilities of Fe_3O_4 and $Ca_{10}P_6O_{25}$ phases in the CaO-SiO_2-FeO-P_2O_5-B_2O_3 melt were quantified with the index of $(T_U-T_I)/T_I$ (where T_I and T_U are the peak temperatures of the nucleation rate and growth rate of a phase) and the crystallization ability of magnetite (Fe_3O_4) was found to be larger than that of calcium phosphate ($Ca_{10}P_6O_{25}$) phase. The optimum temperature range for the crystallization of magnetite (Fe_3O_4) and calcium phosphate ($Ca_{10}P_6O_{25}$) phases was optimized subsequently. This study provides necessary information for the recovery and utilization of Fe and P from steelmaking slag, by selectively precipitating Fe and P rich phases.

Key Words: Steelmaking slag; Magnetite (Fe_3O_4); Calcium phosphate ($Ca_{10}P_6O_{25}$); Nucleation and growth; Kinetics

1. Introduction

Steelmaking slag is one of the main by-products from the iron and steel making process.

The conversion rate of steelmaking slag is approximately 10-15% per ton of steel produced. The major components in steelmaking slag are CaO, SiO_2, and Fe_tO but they also contain some valuable oxides such as P_2O_5 and MnO. Steelamking slags are considered potential sources for road construction [1], cement [2], ceramics [3-6], fertilizer [7], civil engineering projects [8] as well as feedstock for re-use in the steelmaking process. However, the technical and environmental obstacles for some steelmaking slags in the above applications, such as volumetric expansion [9], disintegration [10], leaching of metals [11] and reverse of phosphorus to the hot metal [12], result in the insufficient recycling rate of steelmaking slags. Besides, the nonmagnetic valuable oxides, such as FeO and P_2O_5, in steelmaking slags in the conventional applications from the slag are not recovered. With an increase in the environmental burden and depletion of natural resources, the extraction of valuable elements from steelmaking slag has drawn significant attention.

Targeting the recovery of valuable oxides from steelmaking slags, several metallurgical processes have been developed to recovery iron from the slags, such as the reduction of iron oxide to metallic Fe using C [13], CO [14], and H_2 [15] and the oxidation of FeO to Fe_3O_4 using air [16-18], and H_2O [19-21], followed by magnetic separation. However, the reduction methods suffer from some limitations and reducing conditions are likely to promote phosphorus reversion to the hot metal [22]. When considering oxidation routes which may enable efficient selective recovery of iron oxide from steelmaking slags, the selective precipitation Fe_3O_4 could allow for subsequent separation since the phase is magnetically susceptible. For phosphorus recovery from steelmaking slag, various technologies have been developed, such as flotation [23], magnetic

separation [24], super gravity separation [25-27], reduction [28-30], leaching [31-33] and a three-stage continuous-selective process (selective enrichment-selective growth-selective separation) [34-36]. The above-mentioned technologies provide, to some degree, better understanding of the phosphorus-containing phase formation to remove or extract phosphorus from steelmaking slags, and the three-stage continuous selective process is regarded as the most promising process due to its high efficiency and low waste emission.

Based on the three-stage continuous selective process, a preliminary study on selectively enriching iron and phosphorus in the form of magnetite (Fe_3O_4) and calcium phosphate ($Ca_{10}P_6O_{25}$) phases by controlling oxygen partial pressure and adding slag modifier of B_2O_3 have been reported by the current author [37]. Of the three steps, the second step of optimizing conditions to facilitate the growth of magnetite (Fe_3O_4) and calcium phosphate ($Ca_{10}P_6O_{25}$) phases in phosphorus-containing slags plays a key role for the subsequent technical step of selective separation, and therefore, the present work aims at investigating the crystallization behavior of the synthetic molten CaO-SiO_2-FeO-P_2O_5-B_2O_3 slag. Specifically, the isothermal temperature on the detailed crystallization properties, morphologies and crystal phases were determined by in situ observation via confocal scanning laser microscope, characterization through SEM-EDS and XRD, while the kinetics of nucleation and growth of iron- and phosphorus-rich phases have been calculated by a classical crystallization kinetic model.

2. Experimental methods

2.1. Materials and sample preparation

The chemical composition of synthetic slags was presented in **Table 1** with the P_2O_5

content being 10%. The chemical reagents of CaO and SiO_2 were dried at 1000 ℃ for 4 hours under Ar atmosphere to remove the small amount of volatiles and hydrones. The synthetic slag was made in a platinum crucible by heating the mixture of chemical reagents of CaO, SiO_2, P_2O_5 and FeO at 1600 ℃ in a vertical tube furnace for 2 hours under high purity Ar atmosphere (99.999%) at the flow rate 0.5 L/min, and then the synthesized slag was rapidly quenched into water. The quenched slag sample was ground to slag powder which is henceforth denoted as pre-melted slags. As shown in **Table 1**, the composition measured by XRF was generally in agreement with the designed composition within the relative difference of 5 pct.

Table 1 Chemical composition of the synthesized slag

	CaO	SiO_2	FeO	P_2O_5	B_2O_3
Designed	34.29	13.71	36	10	6
Measured	33.77	12.98	37.87	10.06	5.32

2.2. Experimental apparatus and procedure

To determine the crystallization temperature of different phases, the crystallization event was in-situ observed optically under the high temperature confocal laser scanning microscope (CLSM) (SVF-SP; Yonekura MFG. Co. LTD, Japan), and recorded at various temperatures in an Ar atmosphere. Before the experiment, the CLSM chamber was evacuated for 10 minutes and was purged with argon gas for 10 minutes. After that, 0.2 g of the slags was placed in a Pt crucible and then heated at the hot stage of CLSM under Ar atmosphere. The thermal cycle employed in the isothermal experiment is shown in **Fig. 1**. To ensure the slag fully melted, the sample was maintained at 1600 ℃ for 5 minutes. The molten slag sample was then quenched at a cooling rate of 50 ℃/s to a preset temperature and held for 5-30 minutes to construct the TTT (Time Temperature Transformation) diagram, through analyzing variations of crystalline fraction with time

and temperature. To identify the microstructure, element distribution and mineral components, the samples were quenched from different temperatures and characterized by scanning electron microscopy equipped with energy disperse spectrum (EDS; ZEISS EVO 18) and determined by X-ray diffraction (TTRIII from Rigaku Corporation).

3. Calculation

3.1. Analytical model

According to the crystallization behavior of the $CaO\text{-}SiO_2\text{-}FeO\text{-}P_2O_5\text{-}B_2O_3$ melt observed in situ by means of confocal scanning laser microscope in the section of "4.1 Visualization of crystallization and phase characterization", the crystallization of magnetite (Fe_3O_4) and calcium phosphate ($Ca_{10}P_6O_{25}$) phases in the slag can be divided into two stages: nucleation and growth. Based on theories of nucleation and absolute rate, the classic crystallization kinetic model can be expressed by Equation (1) and (2) for the nucleation and growth rate of crystals in a supercooled liquid [38-41].

$$I = N_0 kT(3\pi a^3\eta)^{-1}\exp[-\,b\alpha^3\beta(\Delta T_r^{\,2}T_r)^{-1}] \quad (1)$$

$$U = fkT(3\pi a^2\eta)^{-1}\left[1-\exp\left(\frac{-\beta\Delta T_r}{T_r}\right)\right] \quad (2)$$

where I and U are the nucleation and growth rate respectively; N_0 is the number of molecules (or atoms) per unit volume; k is Boltzmann's constant; T is the absolute temperature; a is the lattice parameter of the crystal; η is the viscosity; b is a constant determined by the nucleus shape and for spherical nuclei, $b=\frac{16\pi}{3}$; T_r and ΔT_r are the reduced temperature and undercooling, which are defined as: $T_r=\frac{T}{T_m}$ and $\Delta T_r = 1-T_r$ respectively; f is the fraction of acceptor sites in the crystal surface, and f can be given by Eq. (3); α and β are the reduced crystal/liquid interfacial tension and reduced molar heat

of fusion, which are defined as Eq. (4) and Eq. (5) respectively.

$$f = \begin{cases} 1 & \Delta H_m < 2RT_m \\ 0.2\Delta T_r & \Delta H_m > 4RT_m \end{cases} \quad (3)$$

$$\alpha = \frac{\sigma (V^2 N_A)^{1/3}}{\Delta H_m} \quad (4)$$

$$\beta = \frac{\Delta H_m}{R T_m} \quad (5)$$

where σ is the crystal/liquid interfacial tension; N_A is Avogadro's constant; R is the gas constant; ΔH_m is the molar heat of fusion; T_m is the melting point of the crystal and V is the molar volume of the crystal.

3.2. Determination of parameters

Our previous study [37] regarding the feasibility of separation and extraction of Fe- and P-rich phases from CaO-SiO_2-FeO-P_2O_5-B_2O_3 slags has reported that, magnetite (Fe_3O_4) and calcium phosphate ($Ca_{10}P_6O_{25}$) phases were the main precipitated phases during the cooling process from 1600 °C to 900 °C. The similar result was obtained in the section of "4.1 Visualization of crystallization and phase characterization" of the current study. The parameters of structure are adopted according to the databases of XRD standard pattern, while the melting temperature is obtained from the reference book [42]. **Table 2** presents the parameters of structure and melting temperature of magnetite (Fe_3O_4) and calcium phosphate ($Ca_{10}P_6O_{25}$) phases.

Table 2 Parameters of structure and melting point of Fe- and P-rich phases [42]

Fe- and P-rich phases	Lattice parameter a, Å	Melting temperature, °C
Magnetite (Fe_3O_4)	8.39	1870
Calcium phosphate ($Ca_{10}P_6O_{25}$)	9.43	2083

It is reported that the reduced molar heat of fusion β lies between 1 and 10 for most substances [39]. Only in a few cases can the interfacial tension (α) between the crystal

and the liquid be directly measured, and there is no specific theory to predict it. Therefore, the values of α and β are referred from other reports [43, 44], i.e. α = 1/3 and β = 1. It should be pointed out that although the magnetite (Fe_3O_4) and calcium phosphate ($Ca_{10}P_6O_{25}$) that are taken into consideration are different materials and their properties related to the values of α and β are different, wide applications of the nucleation kinetic model have shown that the values of α and β are almost the same for crystalline phases in metallurgical melts or slag [45, 46]. Therefore, it is reasonable to regard the α and β values of the magnetite (Fe_3O_4) and calcium phosphate ($Ca_{10}P_6O_{25}$) as the same when there is no specific theory to predict them or no effective method to measure them.

In the current study, the viscosity of the synthesized $CaO\text{-}SiO_2\text{-}FeO\text{-}P_2O_5\text{-}B_2O_3$ slag was calculated by the Arrhenius equation as shown in Eq. (6).

$$\ln\eta = \ln A + \frac{B}{T} \tag{6}$$

Where A and B are constants with respect to temperature, which can be expressed by the National Physical Laboratory model [47] relating the viscosity of slags to the structure through the optical basicity in Eqs. (7) and (8)

$$\ln A = -232.69(\Lambda)^2 + 357.32\Lambda - 144.17 \tag{7}$$

$$\ln\frac{B}{1000} = -1.77 + \frac{2.88}{\Lambda} \tag{8}$$

Where Λ is the optical basicity, and the routine employed for calculating the optical basicity is given by Eq. (9)

$$\Lambda = \frac{\sum \chi_i n_i \Lambda_i}{\sum \chi_i n_i} \tag{9}$$

Where χ_i, n_i and Λ_i are the mole fraction, number of oxygen atoms in the molecule and optical basicity of slag components respectively. The optical basicities of the slag

components that are used for calculation in this work are taken from the literature [47,48] and given in **Table 3**.

Table 3 Values of optical basicities of components of $CaO\text{-}SiO_2\text{-}FeO\text{-}P_2O_5\text{-}B_2O_3$ slag [47, 48]

	CaO	SiO_2	FeO	P_2O_5	B_2O_3
Λ_i	1.0	0.48	1.0	0.4	0.42

4. Results and discussion

4 .1. Visualization of crystallization and phase characterization

The crystallization evolution of the synthesized $CaO\text{-}SiO_2\text{-}FeO\text{-}P_2O_5\text{-}B_2O_3$ slag at 1275 ℃, 1200 ℃ and 1100 ℃ was imaged and the representative images are shown in **Fig. 2-4**, respectively. It can be seen that the nucleus of the primary crystal phase were observed to form when the molten slag was quenched at 50 ℃/s from 1600 ℃ to 1275 ℃ and maintained for 554 s at 1275 ℃ (**Fig**. **2**(a)). The quantity of crystal nuclei increases and the frame of crystal gradually forms with the increasing holding time from 554 s to 1164 s. Thereafter, the volume and growth of the crystal nucleus increasingly extended from the edge to the center of slag sample (**Fi**g. **2**(b)-2(f)). Finally, the crystal forms a faceted morphology that is cantered in the particle marked by the red dotted square (**Fig. 2**(f)). Actually, the crystals tended to have more prevalent faceted morphology when the degree of supercooling was lower, which is in accordance with the observed morphology of molten $CaO\text{-}SiO_2\text{-}FeO\text{-}MnO$ slags reacting with moisture during the isothermal region in our previous investigation [20].

It is interesting to note that, the crystal nucleus, looking like gravel, were observed to form when the molten slag was quenched at 50 ℃/s from 1600 ℃ to 1200 ℃ and maintained for 98 s at 1200 ℃ (**Fig. 3**(a)). With the holding time increasing from 98 s to

137 s, the morphology of crystals transformed from gravel shape into two petal-like crystals (**Fig. 3**(b)), then into a boomerang-shaped morphology (**Fig. 3**(c)), and subsequently into a crab-like pincer shape (**Fig. 3**(d)). Finally, well-balanced and symmetrical clover-patterns, just like the plane when three-dimensional earth expand, started to form at 145 s (**Fig. 3**(e)), accompanying the precipitation of some new crystal nucleus at the gap of clover leaves at 162 s (**Fig. 3**(f)). In summary, with the holding time increasing from 98 s to 162 s, nucleation and growth of crystal appears a dynamic process, which is a transition from non-equilibrium state to equilibrium state and from asymmetric patterns to symmetric ones.

In comparison, a rod-shaped morphology appeared when the molten slag was quenched at 50 ℃/s from 1600℃ to 1100 ℃ and maintained for 61 s at 1100 °C (**Fig. 4**(a)). The rod-shaped crystal grew toward the center of the sample as seen in **Fig. 4**(b), which may suggest that the nucleation of the rod-shaped crystal was heterogeneous nucleation. With the holding time increasing from 357 s to 1084 s, the volume and growth of the crystal nucleus increasingly extended from the edge to the center of slag sample, accompanying the coarsening of rod-shaped crystal (**Fig. 4(**b) -4(f)).

The different phase precipitation sequence at different isothermal temperatures for the CaO-SiO_2-FeO-P_2O_5-B_2O_3 melt could be attributed to some or all of these factors (undercooling [49], slag composition [50] and enthalpy of mixing (so-called Jackson α factor) [51]), which will be reported in a separate paper.

Fig. 5 shows the CLSM morphology of the crystalline in the slag at the isothermal temperature of 1100℃ for 1084 seconds and the corresponding SEM morphology. It is noticeable that these white hexagonally faceted crystals (P1 and P2) were surrounded by

lath-shaped phase (P3 and P4) and slag matrix (P5 and P6), indicating an early crystallization, in comparison to lath-shaped phase and slag matrix. In order to determine the elementary distribution in different phases, EDS mapping analysis was carried out and the corresponding results were presented in **Fig. 6**. The lath-shaped phase was mainly phosphorus, while the white phase was mainly Fe. Moreover, the slag matrix mainly composed of Ca and Si. Accordingly, EDS spot analysis (**Table 4**) indicated that the lath-shaped phase was close to $Ca_2PO_{4.8}$ (or Ca_2PO_4), while the white phase and slag matrix were approaching $Fe_3O_{3.9}$ (or $Fe_3O_{4.2}$) and $CaFe_{0.3}Si_{0.7}O_{2.1}$ (or $CaFe_{0.3}Si_{0.8}O_{2.1}$) respectively.

Table 4 EDS analysis of different phase areas in the slag at 1100 ℃, corresponding to **Fig. 5**(d) (Wt.%)

	Ca	Si	O	P	Fe	Potential Formula
P1	41.87	1.25	40.01	16.87	--	$Ca_2PO_{4.8}$
P2	44.28	2.43	35.74	17.55	--	Ca_2PO_4
P3	1.19	--	26.71	--	72.1	$Fe_3O_{3.9}$
P4	2.88	0.53	27.64	--	68.95	$Fe_3O_{4.2}$
P5	36.28	17.83	31.13	0.55	14.21	$CaFe_{0.3}Si_{0.7}O_{2.1}$
P6	35.03	18.53	29.59	--	16.85	$CaFe_{0.3}Si_{0.8}O_{2.1}$

--The amount of the phase is below the lower detection limit

The X-ray energy of element B is too low to detect, so B is not listed in **Table 4**

Isothermal experiments were carried out in a wide temperature range of 1000-1300 ℃ to construct TTT diagram for the onset of crystallization of the synthesized slag. The time for the beginning of crystallization was assumed to be the temperature when the crystal nucleus first came into the sight under CLSM observation although the crystal nucleus might form ahead of the observation due to the limited resolution of CLSM.

Fig. 7 showed the TTT diagram of the synthesized $CaO\text{-}SiO_2\text{-}FeO\text{-}P_2O_5\text{-}B_2O_3$ slag. As can be seen, the TTT diagram presents a double C shape and is divided into two regions above and below 1150 ℃. This may suggest that there were two different nucleation

events in the crystallization process of the synthesized CaO-SiO_2-FeO-P_2O_5-B_2O_3 slag and that the crystal morphology drastically changed around 1150 ℃. In order to identify the crystalline phases formed in the two different regions, the slags quenched from 1200 ℃ and 1100 ℃ were selected as a representative for the 'double C shape' slag to confirm crystalline phases using XRD. **Fig. 8** shows the XRD results in the 'double C shape' slag, indicating that the crystallization phases change significantly with decreasing the temperature. In a relatively higher-temperature section ranged from 1300 ℃ to 1150 ℃, the crystalline phase was only Fe_3O_4. With decreasing the isothermal temperature to below 1150 ℃, $Ca_{10}P_6O_{26}$ phase precipitated and the crystalline phases in the slag composed of both $Ca_{10}P_6O_{26}$ and Fe_3O_4 in the temperature range of 1150 ℃ to 1000 ℃.

In addition, it is clear that the crystallization incubation time of molten synthesized CaO-SiO_2-FeO-P_2O_5-B_2O_3 slag become shorter when the temperature changes from 1300 ℃ to 1200 ℃ and from 1150 ℃ to 1100 ℃ (in **Fig. 7**), indicating that the lower the temperature, the easier the crystallization. The reason could be attributed to the supercooling degree for crystallization of slag is insufficient [52]. Therefore, the crystallization is easier with the decrease of temperature. However, the incubation time of crystals is longer when the temperature changes from 1200 ℃ to 1150 ℃ and from 1100 ℃ to 1000 ℃. This is probably because the temperature is too low and the ions in the melt are difficult to move and nucleate. From the results of TTT (in **Fig. 7**) and XRD (in **Fig. 8**), we can find that temperature is a key parameter to control the crystallization of molten slag. In order to recover iron and phosphorus in the form of magnetite (Fe_3O_4) and calcium phosphate ($Ca_{10}P_6O_{25}$) phases from synthesized CaO-SiO_2-FeO-P_2O_5-B_2O_3 slag, it is necessary to investigate the optimum temperature range for the crystallization

of magnetite (Fe_3O_4) and calcium phosphate ($Ca_{10}P_6O_{25}$) phases, which will be discussed in the section of "4.2 Nucleation and growth kinetics of Fe- and P-rich phases".

4.2. Nucleation and growth kinetics of Fe- and P-rich phases

Targeting the recovery of iron and phosphorus from the synthesized CaO-SiO_2-FeO-P_2O_5-B_2O_3 slag, the kinetics for nucleation and growth of Fe- and P-rich phases is key, since the proportion and grain size of Fe- and P-rich phases has a significant effect on designing any subsequent iron and phosphorus separation process. Based on the kinetic model in current study, the nucleation and growth rates of magnetite (Fe_3O_4) and calcium phosphate ($Ca_{10}P_6O_{25}$) phases were calculated and shown in **Fig. 9 and Fig. 10**. In general, there is a peak in both nucleation and growth rates for magnetite (Fe_3O_4) and calcium phosphate ($Ca_{10}P_6O_{25}$) phases, which is in accordance with the fact that nucleation and crystal growth rate were influenced by two contradictory factors, i.e. the degree of supercooling and the diffusive mass transfer in the synthesized CaO-SiO_2-FeO-P_2O_5-B_2O_3 slag. Taking calcium phosphate ($Ca_{10}P_6O_{25}$) phase as an example, the nucleation and growth rates first increased and then decreased with decreasing isothermal temperature, with the maximum of $0.5\times10^{26} m^{-3}s^{-1}$ at 876°C and $5.57\times10^{-4} ms^{-1}$ at 996°C respectively.

In order to estimate the ability of a substance to form an amorphous/crystal solid, Wu [53] proposed that crystallization abilities of precipitated phases can be expressed by $(T_U-T_I)/T_I$, where T_I and T_U are the peak temperatures of nucleation rate and the growth rate. The larger the value of $(T_U-T_I)/T_I$ of the substance, the better its ability to form an amorphous solid. In contrast, the smaller the value of $(T_U-T_I)/T_I$ of the substance, the better its ability to form a crystal solid. Based on the peak temperatures of the nucleation

rate and growth rate in **Fig. 9 and Fig. 10**, the crystallization abilities of magnetite (Fe_3O_4) and calcium phosphate ($Ca_{10}P_6O_{25}$) phases in synthesized CaO-SiO_2-FeO-P_2O_5-B_2O_3 slag were obtained and are given in **Table 5**. It is clear that the values of $(T_U-T_I)/T_I$ of the magnetite (Fe_3O_4) and calcium phosphate ($Ca_{10}P_6O_{25}$) phases are relatively small, and the value of magnetite (Fe_3O_4) is smaller than that of calcium phosphate ($Ca_{10}P_6O_{25}$) phase, indicating the larger crystallization ability of magnetite (Fe_3O_4) compared to calcium phosphate ($Ca_{10}P_6O_{25}$) phase in the synthesized CaO-SiO_2-FeO-P_2O_5-B_2O_3 slag.

Table 5 Crystallization abilities of magnetite (Fe_3O_4) and calcium phosphate ($Ca_{10}P_6O_{25}$) phases in the synthesized CaO-SiO_2-FeO-P_2O_5-B_2O_3 slag

	T_I, °C	T_U, °C	$(T_U-T_I)/T_I$
Magnetite (Fe_3O_4)	1083	1140	0.0526
Calcium phosphate ($Ca_{10}P_6O_{25}$)	876	996	0.1370

However, the different peak temperatures of the nucleation rate and growth rate between magnetite (Fe_3O_4) and calcium phosphate ($Ca_{10}P_6O_{25}$) phase make it difficult to give an accurate optimum temperature range for the precipitated phases in the synthesized CaO-SiO_2-FeO-P_2O_5-B_2O_3 slag. Fortunately, Johnson and Mehl [54] derived expressions as shown in Eq. (10) for the transformed fraction as a function of time for phase changes that proceed by the formation of nuclei and the growth of these nuclei.

$$f(t)=1-\exp\left(-\frac{\pi}{3}IU^3t^4\right) \tag{10}$$

Herein, the crystallization rate r is defined in Eq. (11).

$$r=\frac{\pi}{3}IU^3 \tag{11}$$

Assumpting that Fe and P only existing in the form of magnetite (Fe_3O_4) and calcium phosphate ($Ca_{10}P_6O_{25}$) phases in the synthesized CaO-SiO_2-FeO-P_2O_5-B_2O_3 slag, and the total crystallization rate r_{Total} (in Eq. (12)) is defined by a function of the crystallization rates of the magnetite (Fe_3O_4) and calcium phosphate ($Ca_{10}P_6O_{25}$) phases in the slag.

$$r_{\text{Total}} = \sum_{i=1}^{2} w_i r_i \quad (12)$$

where w_i and r_i are the mass fraction and crystallization rate of the magnetite (Fe_3O_4) and calcium phosphate ($Ca_{10}P_6O_{25}$) phases respectively. The mass fraction of the magnetite (Fe_3O_4) is 0.636, while that of calcium phosphate ($Ca_{10}P_6O_{25}$) is 0.364.

It can be seen from **Fig. 11** that the total crystallization rate is dominated by magnetite (Fe_3O_4) crystals, which agrees well with the crystallization abilities of magnetite (Fe_3O_4) and calcium phosphate ($Ca_{10}P_6O_{25}$) phases estimated by $(T_U-T_I)/T_I$ in **Table 5**. In other words, the suitable temperature range for the crystallization of magnetite (Fe_3O_4) and calcium phosphate ($Ca_{10}P_6O_{25}$) phases in the synthesized CaO-SiO_2-FeO-P_2O_5-B_2O_3 slag is enhanced by the precipitation of magnetite (Fe_3O_4). More importantly, the precipitation sequence of the magnetite (Fe_3O_4) and calcium phosphate ($Ca_{10}P_6O_{25}$) phases can be deduced from **Fig. 11**. Specifically, precipitation of magnetite (Fe_3O_4) is ahead of calcium phosphate ($Ca_{10}P_6O_{25}$) in the synthesized CaO-SiO_2-FeO-P_2O_5-B_2O_3 slag, which is in accordance with the precipitation sequence of precipitated phases observed by CLSM in **Figs. 2-4**. It should be pointed out that although the values of calculated nucleation and growth rate depend on the values of the model parameters, the calculated crystallization abilities of magnetite (Fe_3O_4) and calcium phosphate ($Ca_{10}P_6O_{25}$) in the synthesized CaO-SiO_2-FeO-P_2O_5-B_2O_3 slag keep to the same order, and the precipitation sequence is the same regardless of the actual values of properties like viscosity, interfacial tension and heat of fusion. As shown in **Fig. 11**, the peak temperature of the total crystallization rate is 1055 ℃, and the optimum temperature range for the crystallization of magnetite (Fe_3O_4) and calcium phosphate ($Ca_{10}P_6O_{25}$) phases is defined as 1055±25 ℃, i.e. 1080℃-1030 ℃.

Based on the investigation results in the current study, an optimized heat treatment condition illustrated in **Fig. 12** for the synthesized CaO-SiO_2-FeO-P_2O_5-B_2O_3 slag can be proposed to obtain magnetite (Fe_3O_4) and calcium phosphate ($Ca_{10}P_6O_{25}$) phases with a

larger size. In **Fig. 12**, θ represents the cooling rate, and 1121 ℃ and 964 ℃ are the temperatures corresponding to the maximum crystallization rates of magnetite (Fe_3O_4) and calcium phosphate ($Ca_{10}P_6O_{25}$) phases. In order to facilitate the subsequent selective separation of magnetite (Fe_3O_4) and calcium phosphate ($Ca_{10}P_6O_{25}$) from the synthesized CaO-SiO_2-FeO-P_2O_5-B_2O_3 slag, larger size of magnetite (Fe_3O_4) and calcium phosphate ($Ca_{10}P_6O_{25}$) is preferred since the extraction efficiency of Fe and P strongly depends on crystal size, and the cooling rate of θ_2 and θ_3 should be set at a relatively small value in order to provide enough time for the nucleation and growth of magnetite (Fe_3O_4) and calcium phosphate ($Ca_{10}P_6O_{25}$). In contrast, the precipitation of the silicate phases should be restricted by setting θ_4 at a large value. For the simple application of separating iron and phosphorus from steelmaking slag in industrial practice, B_2O_3 addition should be added into the molten steelmaking slag during slag tapping process in order to recover iron and phosphorus in the form of magnetite (Fe_3O_4) and calcium phosphate ($Ca_{10}P_6O_{25}$) phases, and each slag ladle should hold slag from converter for several heats to give magnetite (Fe_3O_4) and calcium phosphate ($Ca_{10}P_6O_{25}$) enough time to precipitate and grow. Furthermore, the treated slag can be water quenched at a temperature of 964 ℃ to restrict the growth of silicate phases. Finally, the larger size of magnetite (Fe_3O_4) and calcium phosphate ($Ca_{10}P_6O_{25}$) could be selectively separated through a combination of magnetic separation and flotation.

5. Conclusions

In this study, the crystallization behavior of the CaO-SiO_2-FeO-P_2O_5-B_2O_3 melt have been in situ observed by means of confocal scanning laser microscope. Kinetics of nucleation and growth of Fe_3O_4 and $Ca_{10}P_6O_{25}$ phases have been calculated by a classical crystallization kinetic model. The main conclusions are as follows.

(1) Fe_3O_4 with faceted morphology was found as the 1st precipitate phase in the isothermal interval of 1300 ℃-1150 ℃, while $Ca_{10}P_6O_{25}$ with rod-shaped morphology as the 2nd precipitate phase was observed in the isothermal interval of 1150 ℃ -1000 ℃. Accordingly, TTT curve has two C shapes, Fe_3O_4 and $Ca_{10}P_6O_{25}$ had different precipitation temperature range, with the phase transition temperature at 1150 ℃.

(2) The crystallization abilities of Fe_3O_4 and $Ca_{10}P_6O_{25}$ in the CaO-SiO_2-FeO-P_2O_5-B_2O_3 slag were quantified with the index of $(T_U-T_I)/T_I$ and the crystallization abilities of magnetite (Fe_3O_4) is larger than that of calcium phosphate ($Ca_{10}P_6O_{25}$) phase. The optimum temperature range for the crystallization of magnetite (Fe_3O_4) and calcium phosphate ($Ca_{10}P_6O_{25}$) phases is obtained as 1055±25 ℃, i.e. 1080 ℃-1030 ℃ by both theoretical calculation and experiment.

Declaration of competing interest

The authors declare that they have no known competing financial interests or personal relationships that could have appeared to influence the work reported in this paper.

Acknowledgments

This work was supported by Jiangsu University (19JDG011), the Project of the National Natural Science Foundation of China (Nos. 51874272 and 52111540265), and the Open Foundation of State Key Laboratory of Mineral Processing (No. BGRIMM-KJSKL-2022-23).

References

[1] J.F. Li, X.C. Luo, M.K. Sun, W.G. Shen, B. Cao and X.L. Li, Utilization of steel slags in cement industry, Key Eng. Mater. 599 (2014) 98-102.

[2] M.N. Moline, W.A. Calvo, A.G.T. Martinez, P.G. Galliano, Ambient weathering of steelmaking ladle slags, Ceram. Int. 44 (2018), 18920-18927.

[3] Q.S. Wu, Z.C. Huang, Preparation and performance of lightweight porous ceramics using metallurgical steel slag, Ceram. Int. 47 (2021), 25169-25176.

[4] Y.B. Zong, Q.L. Wan, D.Q.Cang, Preparation of anorthite-based porous ceramics using high-alumina fly ash microbeads and steel slag, Ceram. Int. 45 (2019), 22445-22451.

[5] Z.J. Tang, J. Liang, W.H. Jiang, J.M. Liu, F. Jiang, G. Feng, X.B. Lao, H.D. Tang, T. Wang, Preparation of high strength foam ceramics from sand shale and steel slag, Ceram. Int. 46 (2020) 9256-9262.

[6] K. Tabit, H. Hajjou, M. Waqif, L. Saâdi, Effect of CaO/SiO_2 ratio on phase transformation and properties of anorthite-based ceramics from coal fly ash and steel slag, Ceram. Int. 46 (2020) 7550-7558.

[7] L. Lin, Y. Liu, J. Zhi, S. He, X. Li, Z. Hou, L. Zhang, Influence of slag temperature on phosphorus enrichment in P-bearing steelmaking slag, Ironmak. Steelmak. 48 (2021) 1-9.

[8] S. Israel, T. Carlos, A.P. Juan, S. Jesus, T. Pablo, High performance self-compacting concrete with electric arc furnace slag aggregate and cupola slag powder, Appl. Sci. 10 (2020) 773.

[9] L.M. Juckes, The volume stability of modern steelmaking slags, Trans. Inst. Min. Metall. C 112 (2003) 177-197.

[10] F. Engström, D. Adolfsson, Q. Yang, C. Samuelsson, B. Björkman, Crystallization behaviour of some steelmaking slags, Steel research int. 81 (2010) 362-371.

409 [11] J.F.P. Gomes, C.G. Pinto, Leaching of heavy metals from steelmaking slags, Revista
410 de Metalurgia 42 (2006) 409-416.
411 [12] S. Takeuchi, N. Sano, Y. Matsushita, Separate recovery of iron and phosphorus from
412 BOF slags by using Fe-Si alloys, Tetsu-to-Hagane´ 66 (1980) 2050-2057.
413 [13] D.J. Min, J.W. Han, W.S. Chung, A study of the reduction rate of FeO in slag by
414 solid carbon, Metall. Mater. Trans. B 30B (1999) 215-221.
415 [14] F.D. Qiu, E. Mohamed, M. Yousef, H.Y. Sohn, The kinetics of carbon monoxide
416 reduction of magnetite concentrate particles through CFD modelling. Ironmak.
417 Steelmak. 48 (2021) 769-778.
418 [15] H. Aidin, N. Niusha, I. Mikko, F. Timo, A Review on the kinetics of iron ore
419 reduction by hydrogen, Materials 14 (2021) 7450.
420 [16] A. Semykina, J. Nakano, S. Sridhar, V. Shatokha, S. Seetharaman, Confocal
421 microscopic studies on evolution of crystals during oxidation of the FeO-CaO-SiO_2-
422 MnO slags, Metall. Mater. Trans. B 41B (2010) 940-945.
423 [17] A. Semykina, The kinetics of oxidation of liquid FeO-MnO-CaO-SiO_2 slags in air,
424 Metall. Mater. Trans. B 43B (2012) 56-63.
425 [18] A. Semykina, J. Nakano, S. Sridhar, V. Shatokha, S. Seetharaman, Confocal
426 scanning laser microscopy studies of crystal growth during oxidation of a liquid
427 FeO-CaO-SiO_2 slag, Metall. Mater. Trans. B 42B (2011) 471-476.
428 [19] W.J. Duan, Q.N. Yu, T.W. Wu, F. Yang, Q. Qin. The steam gasification of coal with
429 molten blast furnace slag as heat carrier and catalyst: kinetic study, Int. J. Hydrogen.
430 Energ. 41 (2016) 18995-19004.
431 [20] J.C. Li, D. Bhattacharjee, X.J. Hu, D.W. Zhang, S. Sridhar, Crystallization behavior
432 of liquid CaO-SiO_2-FeO-MnO slag in relation to its reaction with moisture, Metall.
433 Mater. Trans. B 50 (2019) 1931-1948.
434 [21] J.C. Li, D. Bhattacharjee, X.J. Hu, D.W. Zhang, S. Sridhar，Z.S. Li, Effects of slag

435 composition on H_2 generation and magnetic precipitation from molten steelmaking
436 slag-steam reaction, Metall. Mater. Trans. B 50 (2019) 1023-1034.
437 [22] B. Malvoisin, F. Brunet, J. Carlut, G. Montes-hernandez, N. Findling, M. Lanson, O.
438 Vidal, J. Bottero, B. Goffe, High-purity hydrogen gas from the reaction between
439 BOF steel slag and water in the 473-673 K range, Int. J. Hydrogen. Energ. 38 (2013)
440 7382-7393.
441 [23] Z.W. Wang, B. Liang, and J. R. Zhang, Experimental study on low temperature
442 flotation recovery of apatite from a magnetic tailings, Appl. Mech. Mater. 3013
443 (2014) 1501-1505.
444 [24] M.Y. Kazuyo, K. Hironari, N. Tetsuya, Recycling effects of residual slag after
445 magnetic separation for phosphorus recovery from hot metal dephosphorization slag,
446 ISIJ Int. 50 (2010**)** 65-70.
447 [25] X. Lan, J.T. Gao, Y. Du, Z.C. Guo, Selective precipitation and in-situ separation of
448 rutile crystals from titanium bearing slag melt in a super-gravity field, J. Alloy.
449 Compd. 731 (2018) 873-880.
450 [26] J.T. Gao, Y. Li, G.L. Xu, F.Q. Wang, Y. Lu, Z.C. Guo. Separation of olivine crystals
451 and borate containing slag from CaO-SiO_2-B_2O_3-MgO-Al_2O_3 system by utilizing
452 super-gravity, ISIJ Int. 57 (2017) 587-589.
453 [27] J.T. Gao, L. Guo, Y.W. Zhong, H.R. Ren, Z.C. Guo, Removal of phosphorus-rich
454 phase from high-phosphorous iron ore by melt separation at 1573 K in a super-
455 gravity field, Int. J. Min. Met. Mater. 23 (2016) 743-750.
456 [28] Y.Y. Zhang, Q.G. Xue, G. Wang, J.S. Wang. Gasification and migration of
457 phosphorus from high-phosphorus iron ore during carbothermal reduction, ISIJ Int.
458 58 (2018) 2219-2227.
459 [29] M. Sugata, T. Sugiyama, S. Kondo, Reduction of FeO in molten slags with solid
460 carbon, ISIJ Int. 14 (1974) 88-95.

461 [30] S. Takeuchi, N. Sano, Y. Matsushita, Separate recovery of iron and phosphorus from
462 BOF slags by using Fe-Si alloys, Tetsu-to-Hagane´ 66 (1980**)** 2050-2057.
463 [31] C.M. Du, X. Gao, S. Ueda, S.Y. Kitamura, Separation and recovery of phosphorus
464 from steelmaking slag via a selective leaching-chemical precipitation process,
465 Hydrometallurgy 189 (2019) 105109.
466 [32] T. Maruoka, N. Shibata, H.Y. Kitamura, Dissolution behavior of di-calcium silicate
467 and tricalcium phosphate solid solution and other phases of steel-making slag in an
468 aqueous solution. High Temp. Mater. Proc. 31 (2012) 329-338.
469 [33] M. Numata, N. Maruoka, S.J. Kim, S. Kitamura, Fundamental experiment to extract
470 phosphorous selectively from steelmaking slag by leaching, ISIJ Int. 54 (2014)
471 1983-1990.
472 [34] H.M. Xue, J. Li, Y.J. Xia, Y. Wan, L.J. Chen, C.J. Lv, Mechanism of phosphorus
473 enrichment in dephosphorization slag produced using the technology of integrating
474 dephosphorization and decarburization, Metals 11 (2021) 216.
475 [35] J.M. Gonzalez, C.J. Penn, S.J. Livingston, Utilization of steel slag in blind inlets for
476 dissolved phosphorus removal, Water 12 (2020) 1953.
477 [36] G.F. Ye, J. Yang, R.H. Zhang, W.K. Yang, H. Sun, Behavior of phosphorus
478 enrichment in dephosphorization slag at low temperature and low basicity, Int. J.
479 Min. Met. Mater. 28 (2021) 66-75.
480 [37] G.X. Li, J.S. Liang, J. Long, D. Guan, Z.S. Li, S. Seetharaman, J.C. Li, 2022. A
481 Novel process for separation of magnetite and phosphorous phases from a CaO-
482 SiO_2-FeO-P_2O_5 slag, ISIJ Int. 62, DOI: 10.2355/isijinternational.ISIJINT-2021-578.
483 [38] D. Turnbull, Formation of crystal nuclei in liquid metals, J. Appl. Phys. 21 (1950)
484 1022-1028.
485 [39] D. Turnbull, Under what conditions can a glass be formed, Contemp. Phys. 10 (1969)
486 473-488.

[40] J.C. Fisher, J.H. Hollomon, D. Turnbull, Rate of nucleation of solid particles in a subcooled liquid, Science 109 (1949) 168-169.

[41] D.R. Uhlmann, A kinetic treatment of glass formation, J. Non-Cryst. Solids 7 (1972) 337-348.

[42] I. Barin, Thermochemical data of pure substances, 3rd ed., Verlagsgesellschaft mbH, Weinheim, 1995.

[43] B. Li, Z.T. Sui, Glass crystallization kinetics of CaO-MgO-Fe_2O_3-Al_2O_3-SiO_2 slags, Chin. J. Mater. Res. 13 (1999) 412-415.

[44] P.X. Zhang, Z.T. Sui, D.M. Luo, R.J. Ma, Study on crystallization kinetics of component containing boron in MgO-B_2O_3-SiO_2-Al_2O_3-CaO slag, Chin. J. Mater. Res. 9 (1995) 66-70.

[45] X. Zhang, B. Xie, J. Diao, X.J. Li, Nucleation and growth kinetics of spinel crystals in vanadium slag, Ironmak. Steelmak. 39 (2012) 147-154.

[46] X. Lan, J.T. Gao, Z.W. Wang, Z.C. Guo. Viscosity of RE-bearing slag systems and kinetics of nucleation and growth for RE-phases, Ceram. Int. 48 (2022) 3304-13310.

[47] K.C. Mills and S. Sridhar, Viscosity of ironmaking and steelmaking slags, Ironmak. Steelmak. 26 (1999) 262-268.

[48] E. Bordes-Richard, Multicomponent oxides in selective oxidation of alkanes theoretical acidity versus selectivity, Top. Catal. 50 (2008) 82-89.

[49] X.F. Lei, X.X. Xue, Preparation, characterization and photocatalytic activity of sulfuric acid-modified titanium-bearing blast furnace slag, Trans. Nonferrous Met. Soc. China 20 (2010) 2294-2298.

[50] Y.B. Zong, D.Q. Cang, Y.P. Zhen, L. Yu，H. Bai, Component modification of steel slag in air quenching process to improve grindability, Trans. Nonferrous Met. Soc. China 19 (2009) 834-839.

[51] G. Chen, J. Chen, J.H. Peng, R.D. Wan, Green evaluation of microwave-assisted leaching process of high titanium slag on life cycle assessment, Trans. Nonferrous Met. Soc. China 20 (2010) 198-204.

[52] W.L. Wang, S.F. Dai, T.S. Zhang, Z.M. Li, Y.J. Xie, Effect of isothermal and cooling rate on crystallization and viscosity of silicomanganese waste slag, Ceram. Int. 47 (2021), 13622-13627.

[53] J.H. Wu, F.Q. Zhang, G.H Chen, A new method to estimate the ability of forming amorphous solids, Phys. Status Solidi A 101A (1987) K1-K3.

[54] W.A. Johnson, P.A. Mehl, Reaction kinetics in processes of nucleation and growth, Trans. Am. Inst. Mining Metall. Pet. Eng. 135 (1939) 416-441.

Figure captions:

Fig. 1. (a) Thermal cycle of isothermal experiment of the synthesized CaO-SiO_2-FeO-P_2O_5-B_2O_3 slag; (b) powder state; (c) liquid state; (d) crystallization state

Fig. 2. Crystallization behavior of the synthesized CaO-SiO_2-FeO-P_2O_5-B_2O_3 slag at 1275 ℃

Fig. 3. Crystallization behavior of the synthesized CaO-SiO_2-FeO-P_2O_5-B_2O_3 slag at 1200 ℃

Fig. 4. Crystallization behavior of the synthesized CaO-SiO_2-FeO-P_2O_5-B_2O_3 slag at 1100 ℃

Fig. 5. Crystal morphology of different phases in the slag at 1100 ℃: (a)275× CLSM image; (b) 300× SEM image; (c) 550× CLSM image; (d) 500× SEM image

Fig. 6. EDS map scanning of synthesized CaO-SiO_2-FeO-P_2O_5-B_2O_3 slag quenched from 1100℃

Fig. 7. TTT diagram of synthesized CaO-SiO_2-FeO-P_2O_5-B_2O_3 slag

Fig. 8. XRD patterns of the samples quenched from 1200 ℃ and 1100 ℃ respectively

Fig. 9. Nucleation rate of magnetite (Fe_3O_4) and calcium phosphate ($Ca_{10}P_6O_{25}$) phases in synthesized CaO-SiO_2-FeO-P_2O_5-B_2O_3 slag

Fig. 10. Growth rate of magnetite (Fe_3O_4) and calcium phosphate ($Ca_{10}P_6O_{25}$) phases in synthesized CaO-SiO_2-FeO-P_2O_5-B_2O_3 slag

Fig. 11. Crystallization rates of magnetite (Fe_3O_4) and calcium phosphate ($Ca_{10}P_6O_{25}$) phases in synthesized CaO-SiO_2-FeO-P_2O_5-B_2O_3 slag

Fig. 12. (a) Schematic diagram of suitable heat treatment condition; (b) precipitation of Fe_3O_4 phase; (c) precipitation of Fe_3O_4 and $Ca_{10}P_6O_{25}$ phases

Fig. 1. (a) Thermal cycle of isothermal experiment of the synthesized CaO-SiO_2-FeO-P_2O_5-B_2O_3 slag; (b) powder state; (c) liquid state; (d) crystallization state

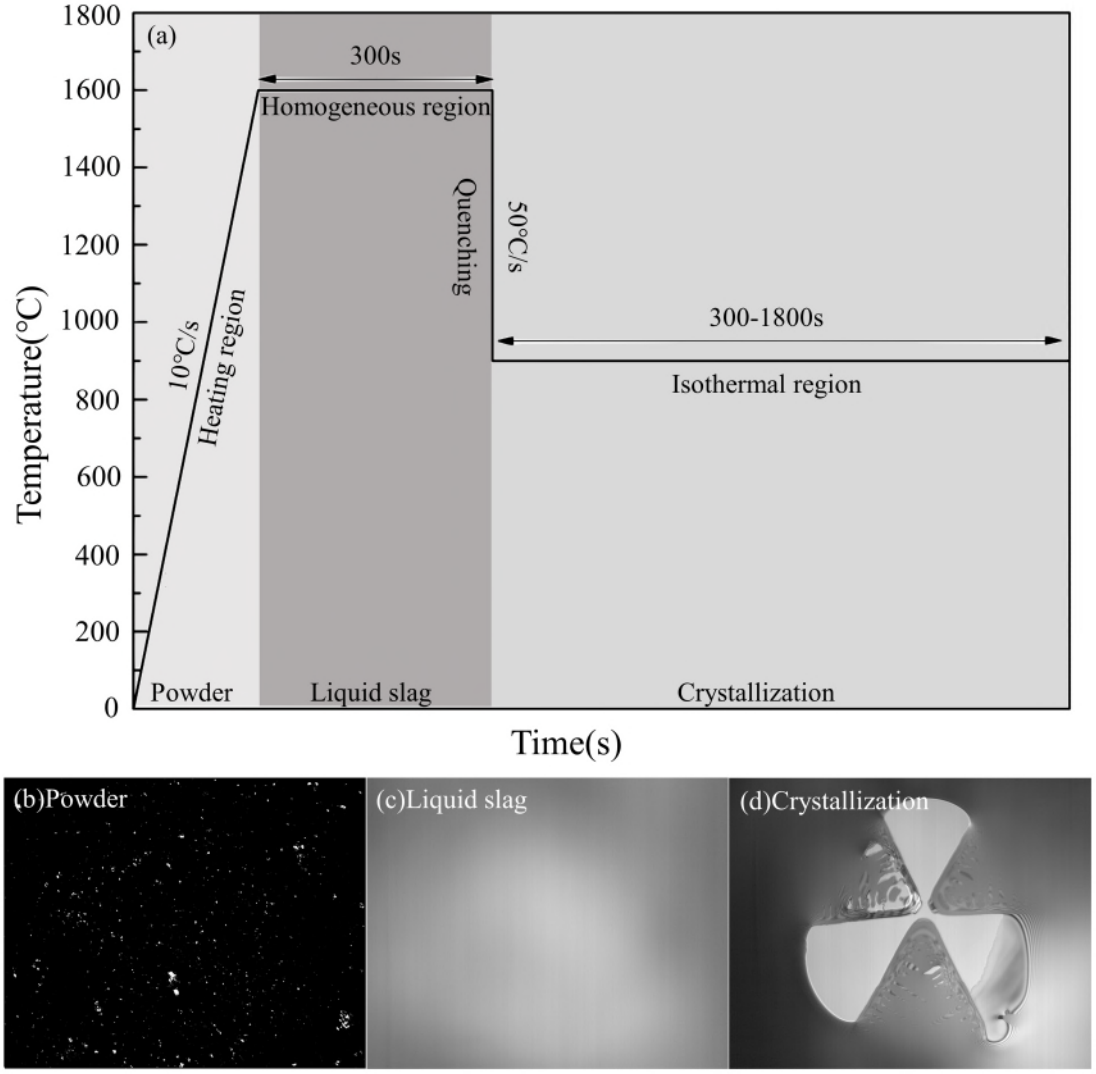

Fig. 2. Crystallization behavior of the synthesized $CaO\text{-}SiO_2\text{-}FeO\text{-}P_2O_5\text{-}B_2O_3$ slag at 1275 ℃

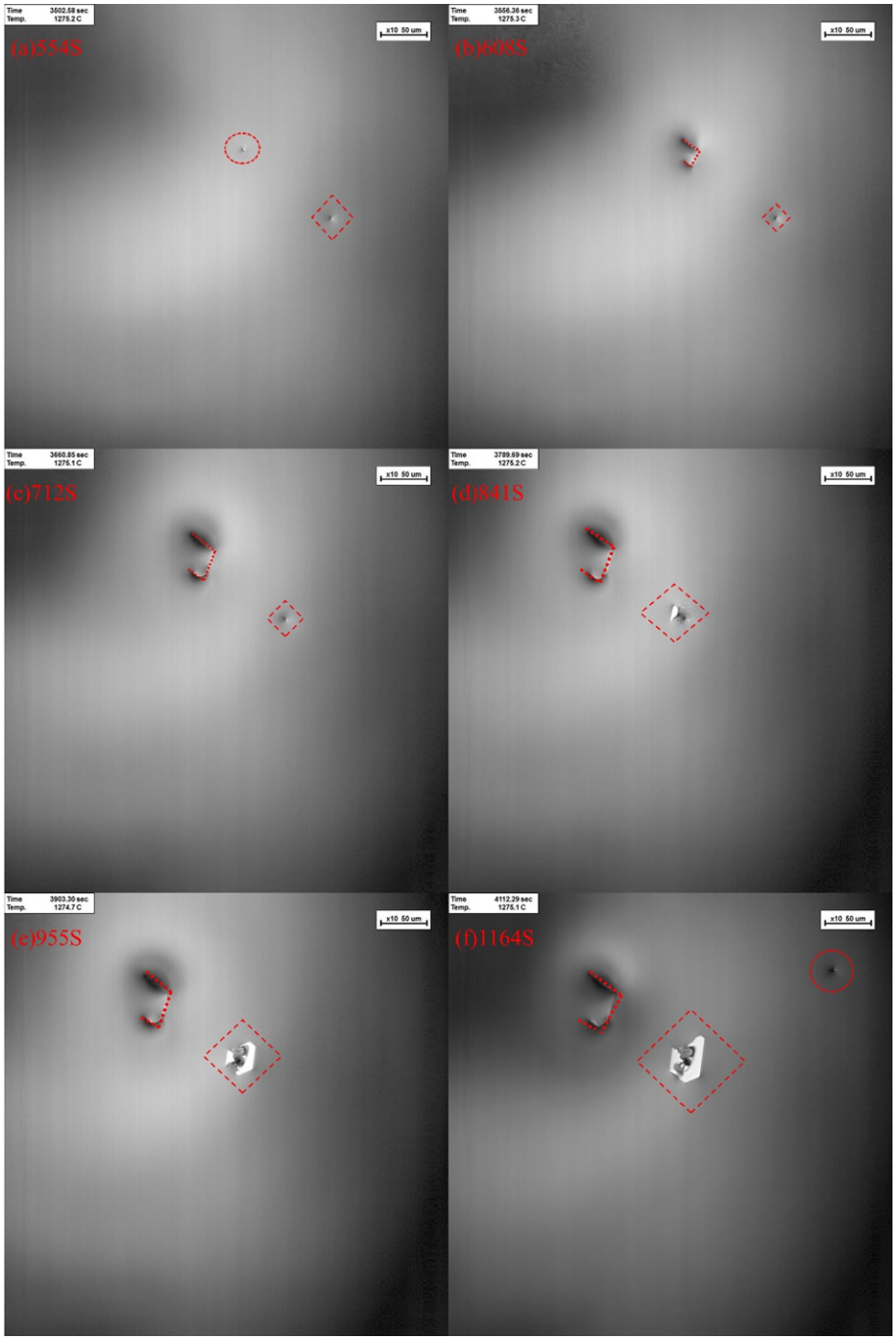

606 **Fig. 3.** Crystallization behavior of the synthesized $CaO\text{-}SiO_2\text{-}FeO\text{-}P_2O_5\text{-}B_2O_3$ slag at
607 1200 ℃

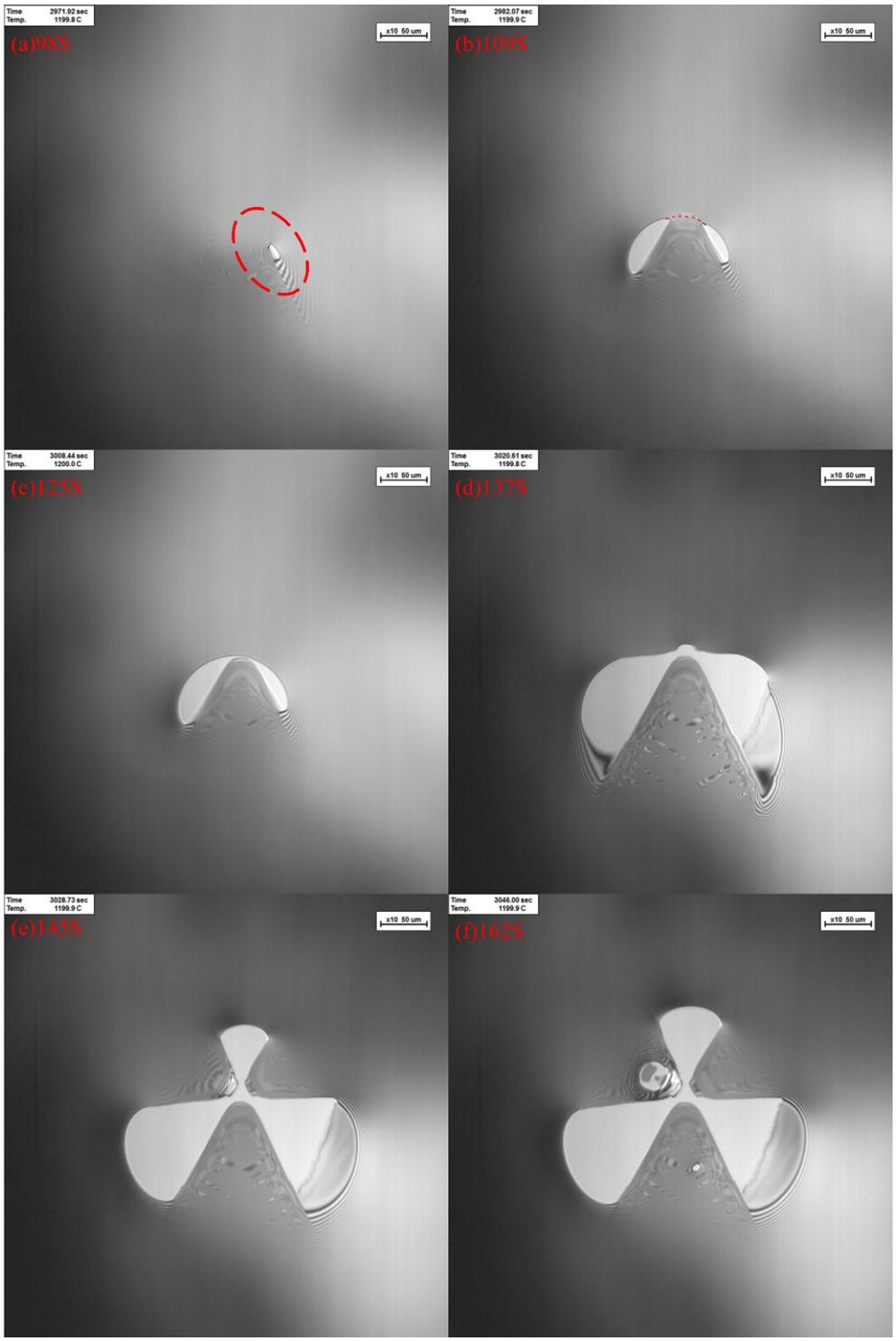

608
609
610
611
612
613
614

615 **Fig. 4.** Crystallization behavior of the synthesized $CaO\text{-}SiO_2\text{-}FeO\text{-}P_2O_5\text{-}B_2O_3$ slag at
616 1100 ℃

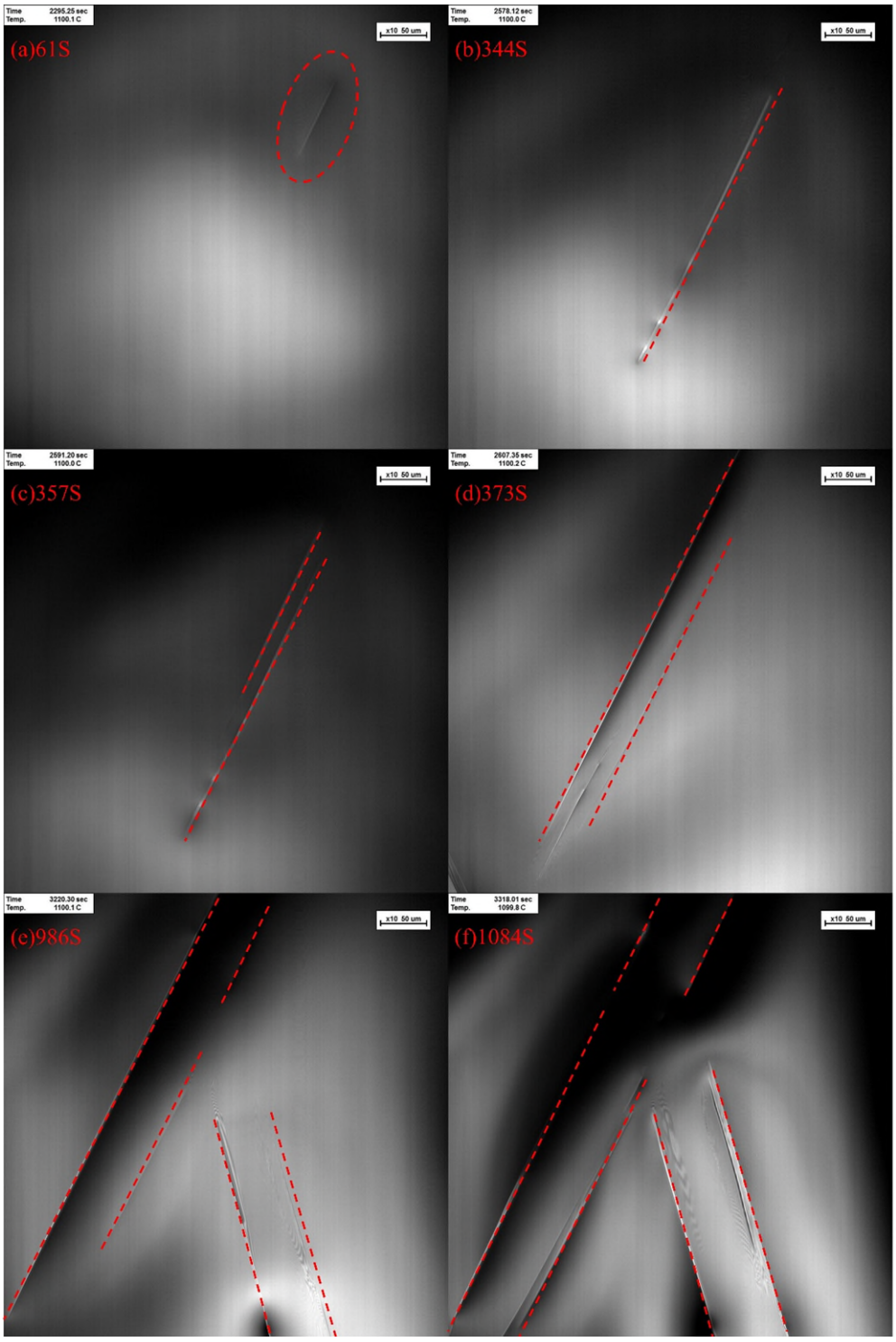

617
618
619
620
621
622
623

Fig. 5. Crystal morphology of different phases in the slag at 1100 ℃: (a)275× CLSM image; (b) 300× SEM image; (c) 550× CLSM image; (d) 500× SEM image

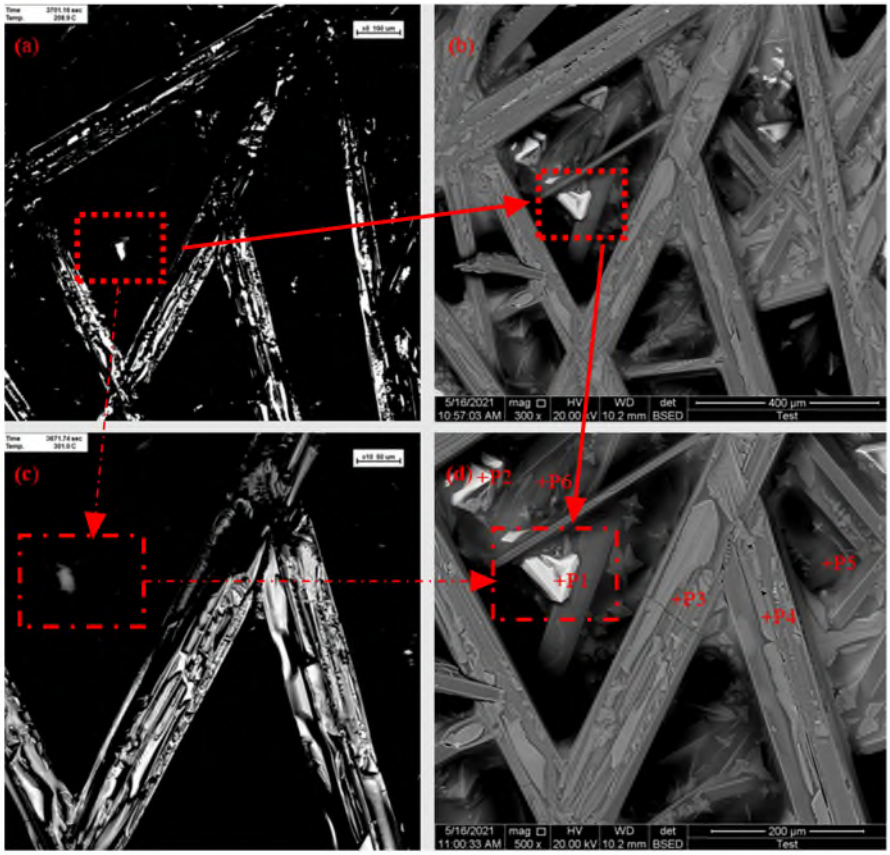

Fig. 6. EDS map scanning of synthesized $CaO-SiO_2-FeO-P_2O_5-B_2O_3$ slag quenched from 1100℃

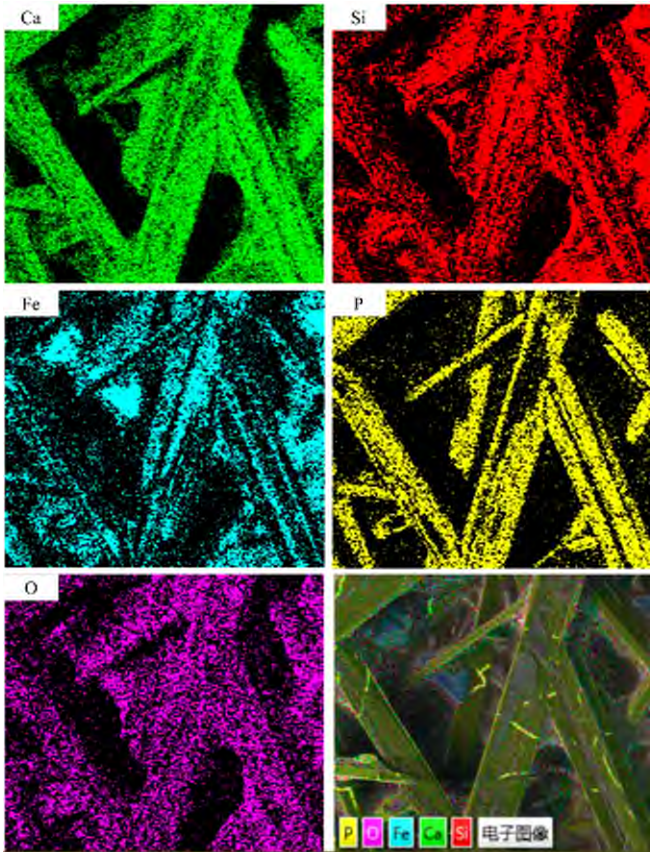

Fig. 7. TTT diagram of synthesized $CaO\text{-}SiO_2\text{-}FeO\text{-}P_2O_5\text{-}B_2O_3$ slag

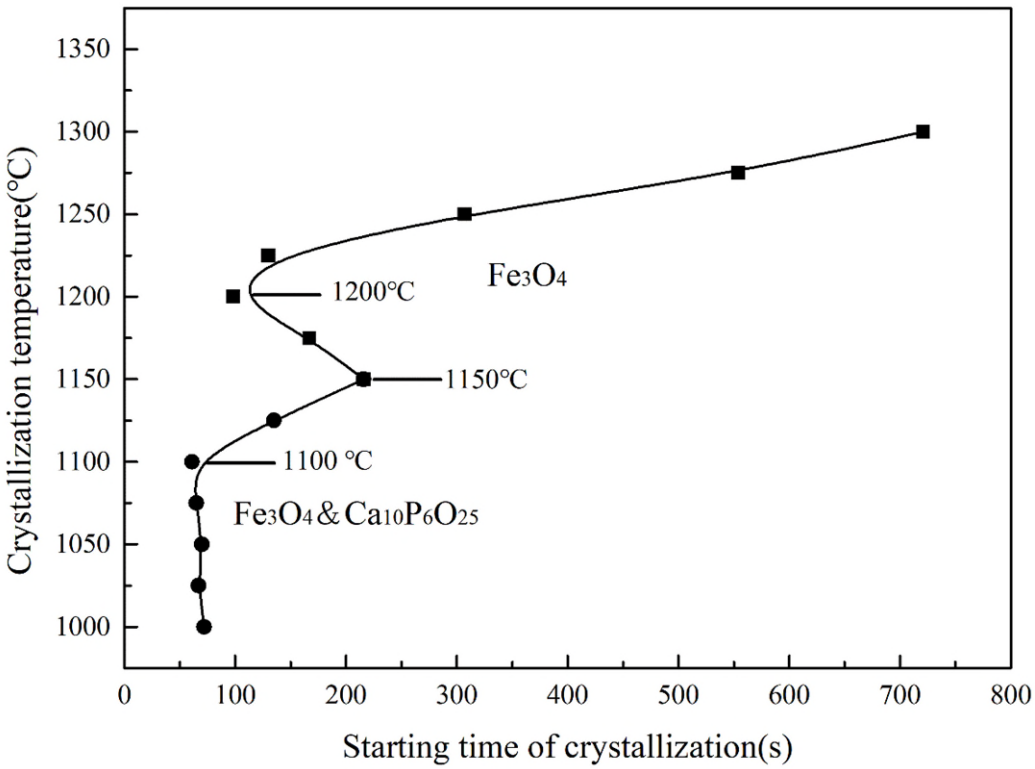

Fig. 8. XRD patterns of the samples quenched from 1200 ℃ and 1100 ℃ respectively

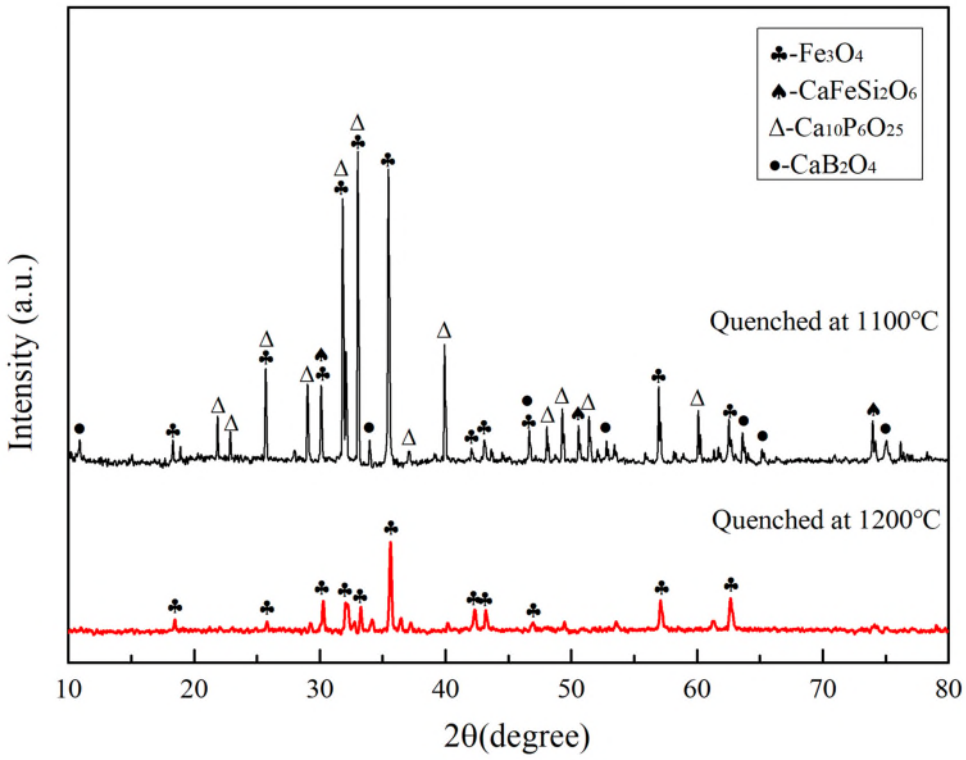

Fig. 9 Nucleation rate of magnetite (Fe_3O_4) and calcium phosphate ($Ca_{10}P_6O_{25}$) phases in synthesized CaO-SiO_2-FeO-P_2O_5-B_2O_3 slag

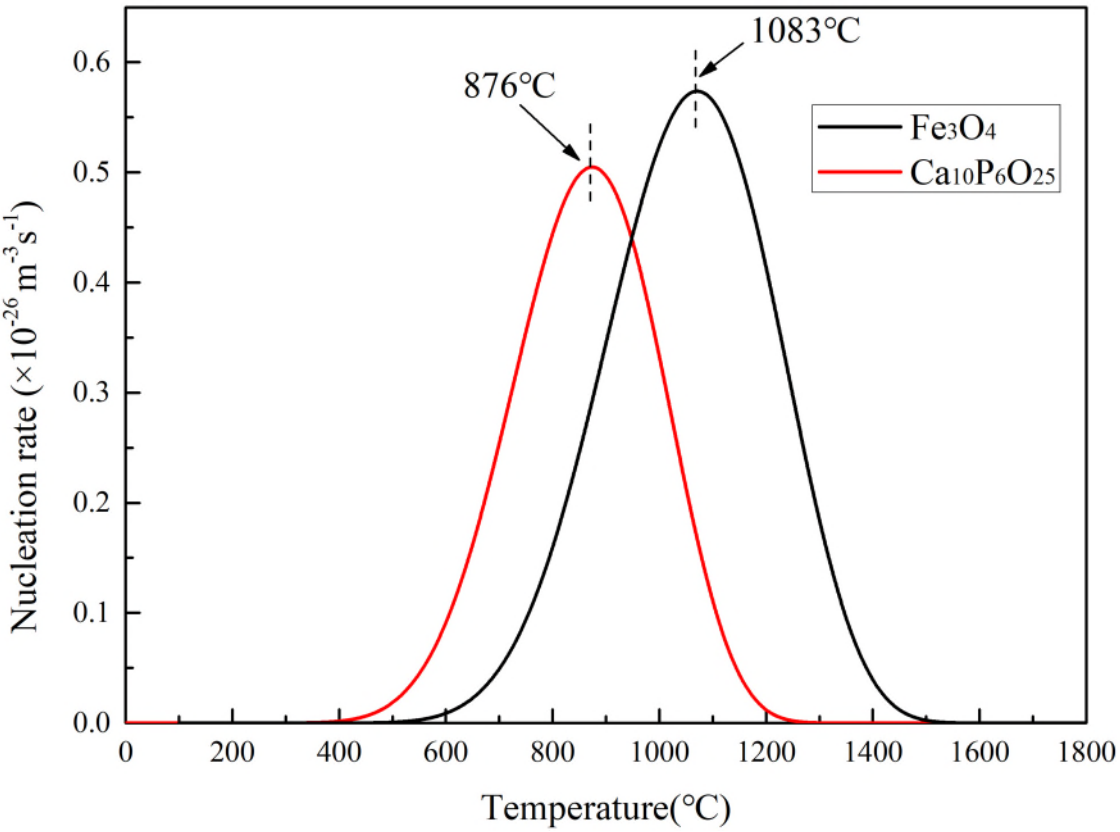

Fig. 10 Growth rate of magnetite (Fe_3O_4) and calcium phosphate ($Ca_{10}P_6O_{25}$) phases in synthesized CaO-SiO_2-FeO-P_2O_5-B_2O_3 slag

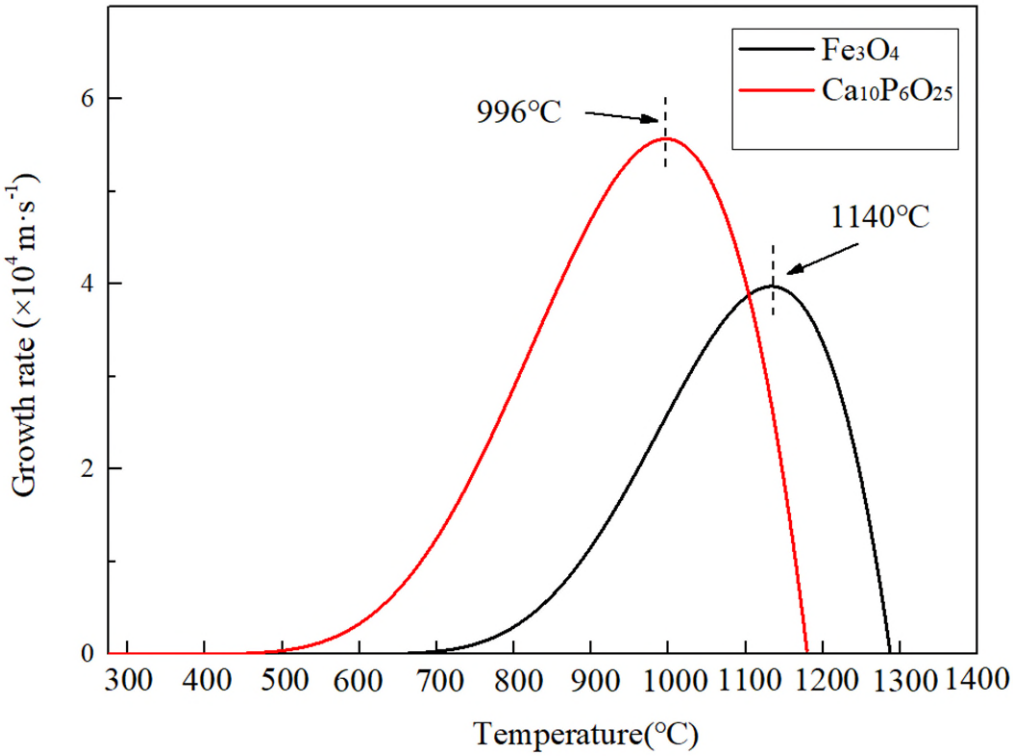

Fig. 11 Crystallization rates of magnetite (Fe_3O_4) and calcium phosphate ($Ca_{10}P_6O_{25}$) phases in synthesized CaO-SiO_2-FeO-P_2O_5-B_2O_3 slag

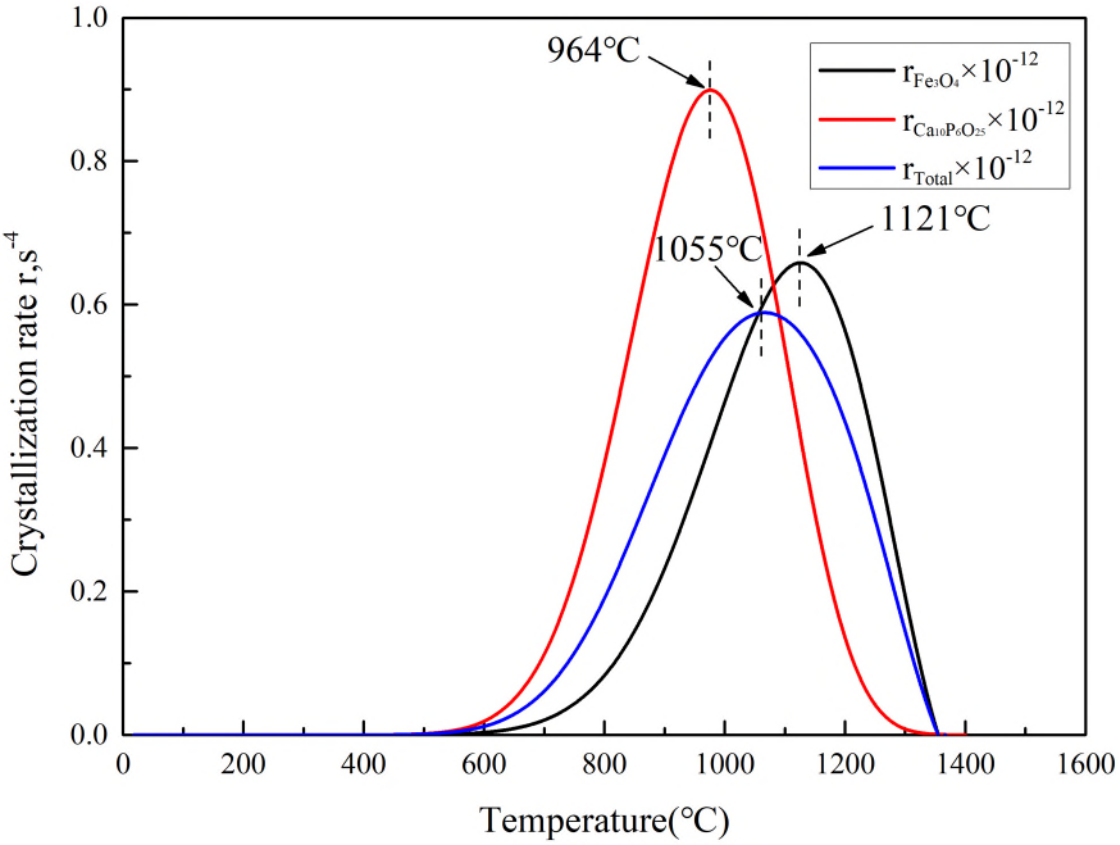

Fig. 12 (a) Schematic diagram of suitable heat treatment condition; (b) precipitation of Fe_3O_4 phase; (c) precipitation of Fe_3O_4 and $Ca_{10}P_6O_{25}$ phases